

# Flip-Chip Packaging of Fluxonium Qubits

Aaron Somoroff,<sup>1</sup> Patrick Truitt,<sup>1</sup> Adam Weis,<sup>1</sup> Jacob Bernhardt,<sup>1</sup> Daniel Yohannes,<sup>1</sup> Jason Walter,<sup>1</sup> Konstantin Kalashnikov,<sup>1</sup> Raymond A. Mencia,<sup>2</sup> Igor V. Vernik,<sup>1</sup> Oleg Mukhanov,<sup>1</sup> Maxim G. Vavilov,<sup>3</sup> and Vladimir E. Manucharyan<sup>2,4</sup>

<sup>1</sup>*SEEQC, Inc., Elmsford, NY 10523*

<sup>2</sup>*Department of Physics, Joint Quantum Institute, and Quantum Materials Center, University of Maryland, College Park, MD 20742, USA*

<sup>3</sup>*Department of Physics and Wisconsin Quantum Institute, University of Wisconsin - Madison, Madison, WI 53706, USA*

<sup>4</sup>*EPFL, CH-1015 Lausanne, Switzerland*

(Dated: March 3, 2023)

The strong anharmonicity and high coherence times inherent to fluxonium superconducting circuits are beneficial for implementing quantum information processors. In addition to requiring high-quality physical qubits, a quantum processor needs to be assembled in a manner that reduces crosstalk and decoherence. In this letter, we report work on fluxonium qubits packaged in a flip-chip architecture. Here, the fluxonium qubits are embedded in a multi-chip module (MCM), where a classical control and readout chip is bump-bonded to the quantum chip. The modular approach allows for improved connectivity between qubits and control/readout elements, and separate fabrication processes. We demonstrate that this configuration does not degrade the fluxonium qubit performance, and identify the main decoherence mechanisms to improve on the reported results.

Superconducting circuits are one of the leading quantum computing platforms due to the orders-of-magnitude growth in coherence times [1, 2] and a path to scalability derived from existing CMOS technologies [3]. To date, superconducting quantum processors composed of many tens of qubits have been demonstrated [4, 5]. A fault-tolerant quantum computer capable of solving classically intractable problems would require millions of physical qubits [6]. This number can be lowered by improving the qubit performance. Nevertheless, the need for scaling up remains.

At present, a major obstacle to scaling is the overhead related to routing the multitude of connections required for qubit control and readout in a planar architecture. The main challenges arise from signal crosstalk between qubits and the conflicting requirement of coupling high-Q qubits to lossier control and readout circuitry [7]. Additionally, we expect that new qubit control methods will be necessary to realize large-scale quantum processors, since the power consumption and physical overhead of conventional analog microwave control is daunting. An example is single flux quantum (SFQ) technology, where the qubits are controlled using digital voltage pulses [8, 9]. In this case, classical SFQ-driving circuits localized on a coprocessor chip at cryogenic temperatures could greatly reduce the level of instrumentation overhead.

A way to scale up from the planar level is to utilize multiple circuit layers; separating the quantum and classical circuitry [10–12]. One approach is the flip-chip package, where a carrier chip that is responsible for qubit control and readout is bump-bonded to the quantum chip (flip-chip), which is flipped such that it faces the carrier. The two chips are separated by vacuum or a chip interposer, and the qubit drive lines and readout resonators couple capacitively to the qubit.

The modular approach allows classical and quantum

elements to be fabricated separately, thereby protecting the qubits from unnecessary exposure to additional fabrication processes. Furthermore, instead of routing signals from the perimeter of the chip, interconnects can be made through its plane, reducing the overlap between individual circuit elements [13]. The flip-chip package is also optimal for digital qubit control using SFQ pulses, where the carrier chip houses active SFQ-driving circuits, since the quasiparticles [14, 15] generated on the carrier by the SFQ-circuits are isolated from the quantum chip [16]. To date, flip-chip packaging has been explored on transmon [17] and capacitively-shunted flux [18, 19] qubits, demonstrating that the qubit performance is not limited in this architecture [20–23].

Over the past decade, the fluxonium circuit [24] has emerged as a promising platform for superconducting quantum computing due to its extremely high coherence and strong anharmonicity [25, 26]. The latter gives fluxonium a clear advantage over the transmon due to the ability to define arbitrarily short gates without the concern of state leakage errors [27]. Recent demonstrations of high fidelity single- and two-qubit gates [28–32] have given way to exploring methods of scaling up fluxonium-based systems [33]. One such method that has not been experimentally realized is embedding fluxonium in a multi-chip module (MCM).

As an initial step, we present results on uncoupled fluxonium qubits embedded on a quantum chip (flip-chip), which is bump-bonded to a carrier chip for control and readout. We demonstrate that the fluxonium qubit performance does not significantly degrade in this new configuration, as compared to previous work on fluxoniums in 2D and 3D [25, 34]. Additionally, we estimate the leading sources of decoherence, and characterize the single qubit gate fidelities in this device.

Our device consists of four uncoupled fluxonium circuits (labelled fluxoniums 1-4, see Figure 1) fabricated

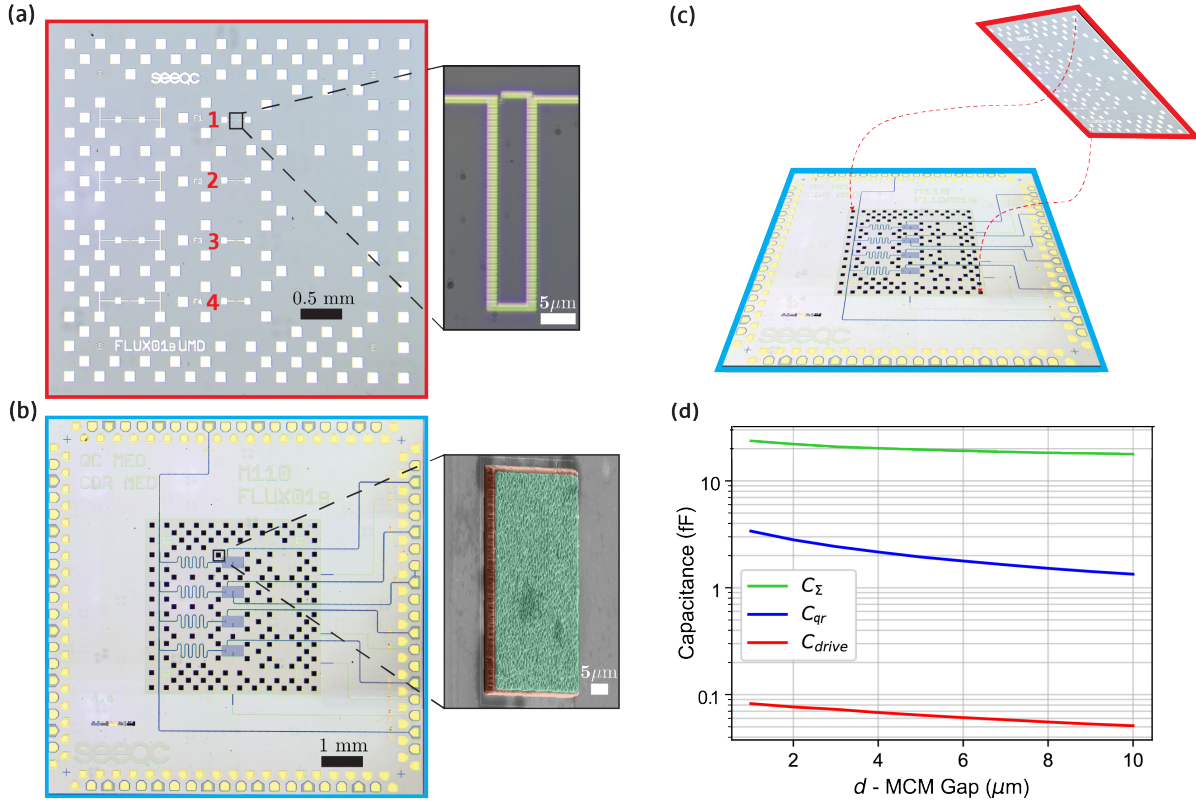


FIG. 1. (a) The  $5 \times 5 \text{ mm}^2$  quantum chip (flip-chip), which houses four uncoupled fluxonium circuits with varying circuit parameters. The Josephson energy  $E_J$  is tuned in each circuit by varying the single phase-slip junction area. The fluxoniums are labelled 1-4 (top to bottom); only fluxoniums 3 and 4 were studied in this work due to their optimal circuit parameters. Aluminum pads are shown, which align with the  $5 \mu\text{m}$  pillars on the carrier chip. Inset is a close-up of a fluxonium circuit. (b) The  $10 \times 10 \text{ mm}^2$  carrier chip housing the classical circuitry for qubit control and readout. A single transmission line couples to four  $\lambda/4$  CPW resonators with fundamental frequencies in the  $6 - 7 \text{ GHz}$  range, which couple to each fluxonium for readout. Additionally, there are four qubit drive lines for XY-rotations of the qubits, and four DC-lines to control the flux bias of the fluxonium loops. Inset is a false-color SEM image of one of the  $120 \times 120 \mu\text{m}^2$  pillars. Orange(green) region is the  $5(1) \mu\text{m}$ -thick aluminum(indium) layer. (c) Schematic of the configuration of flip-chip and carrier chip, which forms the multi-chip module. The flip-chip faces the carrier and the aluminum pads are aligned with the aluminum pillars on the carrier chip. The two chips are then bump-bonded together to construct the MCM (see Supplementary Note 7C). The pads on the carrier chip are wirebonded to a printed circuit board (PCB), which connects to the coaxial cables in the dilution refrigerator (see Supplementary Note 8). (d) Ansys Q3D simulation of total fluxonium shunt capacitance  $C_{\Sigma}$ , fluxonium-resonator coupling capacitance  $C_{qr}$ , and fluxonium-drive line coupling capacitance  $C_{drive}$  versus MCM gap distance  $d$ .

on a silicon chip, which is bump-bonded to the passive carrier chip that houses corresponding microwave control lines and  $\lambda/4$  coplanar waveguide (CPW) resonators [35] for readout. The fluxonium circuit design is the same as in references [25, 26], and can be further optimized for this new packaging method. All four circuits contain 138 large area Josephson junctions in their superinductance arrays. The spectrum of each fluxonium circuit is varied by changing the Josephson energy  $E_J$  to improve the likelihood of hitting an optimal spectrum. For our purposes, we aim for a qubit frequency of around 1 GHz in order to reduce the thermal population in the  $|1\rangle$  state.

Images of the device are shown in Figure 1. The capacitance between the two ends of the fluxonium, as well as to the readout resonator and charge line, was simulated with Ansys Q3D (see Figure 1d). Both ends of the

fluxonium are ungrounded and the capacitance to the carrier groundplane contributes the majority of the fluxonium capacitance. To reduce this capacitance to meet our  $E_C/h = 1 \text{ GHz}$  target, we removed the groundplane from a  $300 \times 600 \mu\text{m}^2$  area of the carrier centered over the fluxonium. To account for the presence of the flip-chip on resonator frequencies, the CPWs that comprise the resonators were simulated with Sonnet.

We extensively characterized fluxoniums 3 and 4 due to their optimal spectra, and focus on fluxonium 3 in the main text. Results on fluxonium 4 are summarized in the Supplementary Material. Dispersive readout of the qubit [36, 37] is performed using the corresponding resonator, capacitively coupled to the fluxonium circuit with empirically determined coupling rate  $g = 2\pi \times 86 \text{ MHz}$ . We begin our analysis of fluxonium

3 by doing one- and two-tone spectroscopy of the resonator and fluxonium (Figures 2a and 2b, respectively). The resulting spectrum in Figure 2 is fit to the bare fluxonium Hamiltonian with the resonator and fluxonium-resonator coupling terms (see Supplementary Note 1). The fit yields Josephson energy  $E_J/h = 2.50$  GHz, inductive energy  $E_L/h = 1.14$  GHz, and charging energy  $E_C/h = 0.89$  GHz. The qubit transition frequency at the half flux quantum (HFQ) operating point (also known as the sweet spot) is  $\omega_{01} = 2\pi \times 1.252$  GHz.

We measured the energy relaxation time  $T_1$  by applying a  $\pi$ -pulse to the qubit and varying the readout delay. At maximum,  $T_1 = 77.3 \pm 7.0$   $\mu$ s (see Figure 3a). The effective dielectric loss tangent  $\tan \delta_C$  corresponding to this maximal  $T_1$  at qubit frequency 1.252 GHz is approximately  $1.6 \times 10^{-6}$  (see Supplementary Note 4). This value is in agreement with previous 3D fluxonium devices fabricated with the same materials and process [25], demonstrating that the switch from 3D to an MCM does not significantly limit  $T_1$  by altering dielectric surface participation ratios [38]. The effect of the MCM configuration on  $T_1$  may vary, however, depending on the carrier groundplane geometry and the inter-chip distance. By optimizing the materials and fabrication process [26, 39], a reduction in  $\tan \delta_C$  by a factor of two is within reasonable expectation.

The coherence time  $T_2$  was measured via Ramsey and Hahn-Echo experiments. In the Ramsey method, two  $\pi/2$ -pulses are applied to the qubit, and the time delay between them is swept. Readout immediately follows the second  $\pi/2$ -pulse. This pulse sequence yields Ramsey fringes with an exponentially decaying envelope with decay constant  $T_2^*$ , the Ramsey coherence time. In the Hahn-Echo sequence [40], a  $\pi$ -pulse is inserted between the two  $\pi/2$ -pulses. This refocusing  $\pi$ -pulse reverses any phase accumulation due to low-frequency drifts during the first half of the sequence [41]. By increasing the number of refocusing  $\pi$ -pulses, known as a Carr-Purcell-Meiboom-Gill (CPMG) sequence [42], the qubit will become more sensitive to noise at successively higher frequencies [43]. At maximum, we measured  $T_2^* = 29.5 \pm 1.1$   $\mu$ s and Hahn-Echo coherence time  $T_2^E = 36.3 \pm 4.0$   $\mu$ s (Figures 3a, c).

We performed an interleaved  $T_1$ ,  $T_2^E$  loop to obtain statistics on the relaxation and coherence times of fluxonium 3, and found  $\langle T_1 \rangle = 55.1 \pm 1.0$   $\mu$ s and  $\langle T_2^E \rangle = 27.5 \pm 1.6$   $\mu$ s. The mean  $T_2^E < T_1$  indicates significant pure dephasing of the qubit. From these mean values, we calculated a corresponding dephasing time of  $T_\phi = 36.6 \pm 2.5$   $\mu$ s. The exponentially decaying Ramsey and Hahn-Echo measurement signals (Figures 3b and c, respectively) indicate that  $1/f$  flux noise [44, 45] is not the predominant dephasing source (see Supplementary Note 5A).

When we applied multiple refocusing pulses in a CPMG sequence, the measured decay time did not increase, indicating dephasing due to white noise (see Supplementary Note 5B). It is therefore most likely that the

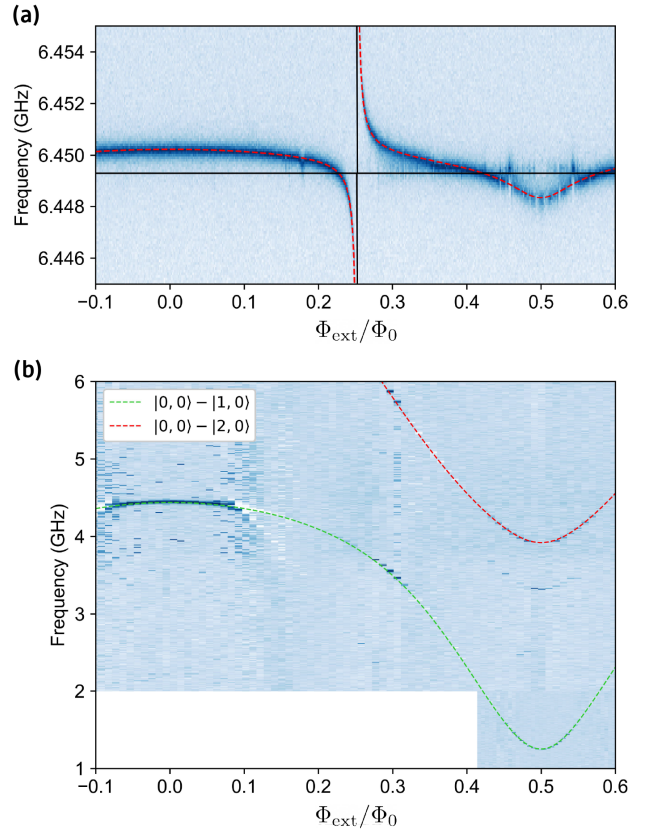


FIG. 2. Spectroscopy of fluxonium 3 over approximately half a flux period. State  $|j, k\rangle$  indicates  $j$  excitations in the fluxonium circuit and  $k$  excitations in the resonator. (a) One-tone spectroscopy of the readout resonator showing the avoided level crossing between the bare fluxonium circuit state  $|2, 0\rangle$  and the fundamental mode of the resonator  $|0, 1\rangle$ . Dashed red curves are the theoretical fit to the coupled fluxonium-resonator Hamiltonian (see Supplementary Note 1), yielding resonator frequency  $\omega_r = 2\pi \times 6.4493$  GHz and resonator-fluxonium coupling rate  $g = 2\pi \times 86$  MHz. For comparison, horizontal and vertical solid black lines are the resonator and bare fluxonium  $|0\rangle - |2\rangle$  transition, respectively, for zero coupling  $g = 0$ . The level splitting between states  $|2, 0\rangle$  and  $|0, 1\rangle$  is given by  $2g|\langle 2|\hat{n}|0\rangle| \approx 2\pi \times 31$  MHz, where  $\hat{n}$  is the charge operator in units of Cooper pairs. (b) Two-tone spectroscopy of the fluxonium circuit depicting the qubit ( $|0, 0\rangle - |1, 0\rangle$ ) and ground to second excited state ( $|0, 0\rangle - |2, 0\rangle$ ) transitions. Dashed curves represent the same fit as in (a), yielding  $E_J/h = 2.50$  GHz,  $E_L/h = 1.14$  GHz,  $E_C/h = 0.89$  GHz. The fainter, unlabelled lines are transitions between higher energy bare fluxonium states  $|j, 0\rangle$  and single resonator excitations  $|0, 1\rangle$ .

pure dephasing of the qubit is caused by thermal photons in the resonator [46]. The dephasing time  $T_\phi = 36.6 \pm 2.5$   $\mu$ s corresponds to an average thermal photon number of  $n_{\text{th}} = (1.2 \pm 0.1) \times 10^{-2}$  and an effective resonator temperature of  $T_{\text{res}} = 70 \pm 1$  mK (see Supplementary Note 3B). Our measured values for  $n_{\text{th}}$  and  $T_{\text{res}}$  agree with those reported on transmon and flux qubits [47, 48].

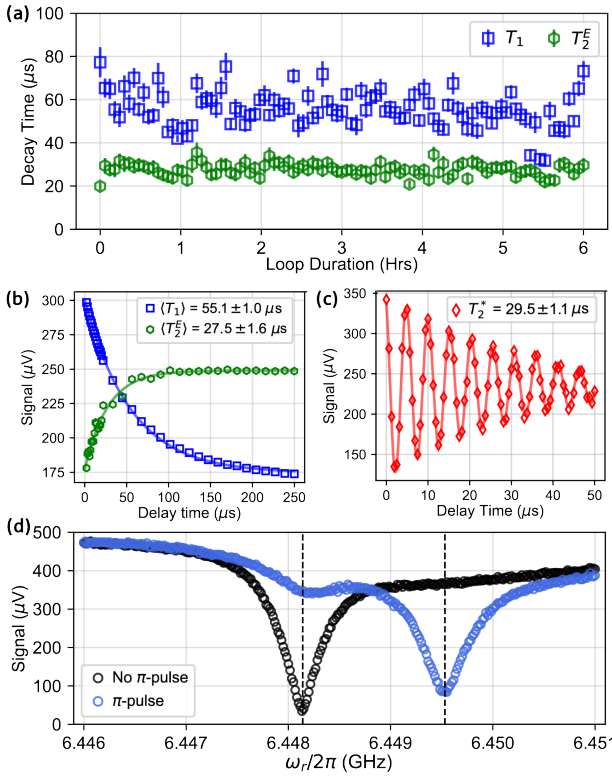


FIG. 3. Measurements of the fluxonium 3 qubit transition taken at the sweet spot  $\Phi_{\text{ext}}/\Phi_0 = 0.5$ . (a) Interleaved energy relaxation time  $T_1$  and Hahn-Echo coherence time  $T_2^E$  loop taken over 6 hours. (b)  $T_1$  and  $T_2^E$  signals averaged over all 101 measurements in loop. The solid curves are the fits to a decaying exponential function. The fitted decay time constants are the mean relaxation time  $\langle T_1 \rangle = 55.1 \pm 1.0 \mu\text{s}$  and Hahn-Echo coherence time  $\langle T_2^E \rangle = 27.5 \pm 1.6 \mu\text{s}$ . (c) A single Ramsey measurement. The solid curve is the fit to an exponentially decaying cosine function, yielding Ramsey coherence time  $T_2^* = 29.5 \pm 1.1 \mu\text{s}$ . (d) One tone spectroscopy of the readout resonator with (light blue data) and without (black data) a single  $\pi$ -pulse applied to the qubit to flip the qubit state. Dashed vertical lines are at the center frequency of each fitted Lorentzian function, and the difference of the two frequencies yields the qubit dispersive shift of  $\chi_{01} = 2\pi \times 1.39 \text{ MHz}$ , in good agreement with the simulated  $\chi_{01}$  (see Supplementary Note 3A).

Lowering the dephasing rate due to thermal photons can be done in two ways. The first directly reduces  $n_{\text{th}}$  by adding attenuation at the readout frequency, which was demonstrated to lower  $T_{\text{res}}$  to below 55 mK [47, 49]. The second method is to lower the ratio of  $\chi_{01}/\kappa$ . In our experiment, we worked in the strong dispersive regime of circuit QED ( $\chi_{01} > \kappa$ ) [50, 51], reaching a regime where  $\chi_{01} \approx \kappa$  is readily achievable simply by lowering  $g$ . For example, reducing  $g$  by a factor of 2 would lower  $\chi_{01}$  by a factor of 4 (see Supplementary Note 3A). Assuming  $T_{\text{res}}$  remains fixed at 70 mK,  $T_\phi$  would rise from 36.6 to 76.9  $\mu\text{s}$ . Additionally, if we improved our readout line attenuation in accordance with the previously cited works, we

can expect a conservative goal of lowering  $T_{\text{res}}$  to 60 mK, corresponding to  $n_{\text{th}} = 0.6 \times 10^{-2}$  and  $T_\phi > 150 \mu\text{s}$ .

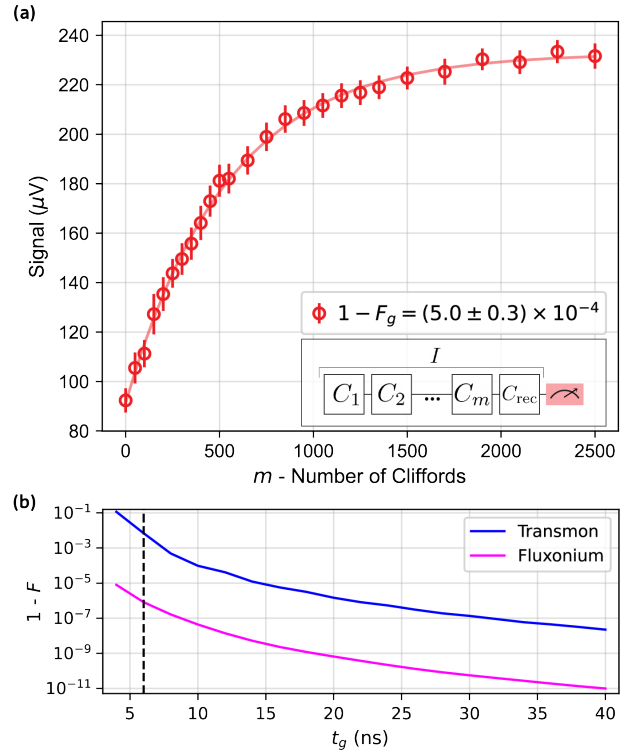


FIG. 4. (a) Single-qubit randomized benchmarking on fluxonium 3. The red data points are the result of averaging over 32 randomizations of the RB sequence. Solid red curve is the fit to the sequence fidelity function  $A + Bp^m$ , yielding an error rate per Clifford of  $r_{\text{cliff}} = (9.2 \pm 0.6) \times 10^{-4}$ . The corresponding fidelity per physical gate generating the Clifford group is  $F_g = 0.99950(3)$ . (b) Simulated bit-flip error rate versus gate duration for fluxonium 3 and a transmon ( $E_J/h = 15 \text{ GHz}$ ,  $E_C/h = 0.3 \text{ GHz}$ ,  $\alpha = -0.345 \text{ GHz}$ ) with no decoherence. Basic (no DRAG), cosine-envelope pulses were used in the simulation (see Supplementary Note 6B). Dashed black line corresponds to the gate duration (6 ns) used in our experiments.

We completed our study of the fluxonium MCM by characterizing the single-qubit gates using randomized benchmarking (RB) [52, 53]. The RB experiment consists of applying  $m$  randomly selected Clifford gates generated by the gate set  $\{I, X, Y, \pm X/2, \pm Y/2\}$ , where we define the identity gate  $I$  as no pulse. Before readout, a final recovery gate is applied after the  $m$  Cliffords such that the full sequence is tantamount to an identity gate (see inset of Figure 4a). This is performed over  $n$  randomizations of the Clifford sequence, and the  $n$  resulting experimental results are averaged together. Due to both coherent and incoherent errors, the measurement signal will decay with the number of Cliffords  $m$  in the sequence as  $A + Bp^m$ , where  $A, B$  are constants absorbing state preparation and measurement (SPAM) errors, and  $p$  is the depolarization parameter. The average error per Clifford gate is  $r_{\text{cliff}} = (1 - p)/2$ , and the corresponding av-

verage error rate per gate generating the Clifford group is  $r_g = r_{\text{cliff}}/1.833$  (since the identity gate is not counted). The average Clifford gate fidelity is then  $F_{\text{cliff}} = 1 - r_{\text{cliff}}$  and the average gate fidelity is  $F_g = 1 - r_g$ .

The physical pulses making up the  $\pm X/2, \pm Y/2$  gates were cosine-envelope microwave pulses with total gate duration  $t_g = 6$  ns. The  $X, Y$  gates were simply two concatenated  $X/2, Y/2$  gates. More information on the pulses and the individual Clifford-generating gate fidelities is found in Supplementary Note 6A. Figure 4a shows the results of the RB experiment on fluxonium 3, along with the fit which yields an average Clifford gate error rate of  $r_{\text{cliff}} = (9.2 \pm 0.6) \times 10^{-4}$ , and an average gate error rate of  $r_g = r_{\text{cliff}}/1.833 = (5.0 \pm 0.3) \times 10^{-4}$ . Given the coherence time of approximately  $T_2^E \approx 30$   $\mu$ s, and the average Clifford gate duration of 13 ns, we estimate the coherence limit for the Clifford gate error rate to be  $4.3 \times 10^{-4}$ . Comparing this estimate to the measured  $r_{\text{cliff}}$ , we conclude that at least half of our gate error can be attributed to imperfect calibration.

Figure 4b shows the simulated bit flip error rate  $1 - F$  versus total gate duration  $t_g$  for fluxonium 3 (anharmonicity  $\alpha = 1.42$  GHz) compared to a transmon ( $E_J/h = 15$  GHz,  $E_C/h = 0.3$  GHz,  $\alpha = -0.345$  GHz), where both systems have no decoherence. The anharmonicity is defined as  $\alpha = \omega_{12} - \omega_{01}$ . The main source of error will then arise from leakage out of the compu-

tational subspace. The simulated gate aims to perform a qubit-flip  $|0\rangle \rightarrow |1\rangle$  with an arbitrary rotation axis. In fluxonium, the lower limit on the bit flip error rate is about 4 orders of magnitude lower than that of the transmon. More details on the simulation are found in Supplementary Note 6B.

In summary, we have packaged fluxonium qubits in a multi-chip module, and demonstrated that there is no significant performance degradation when compared to the previously cited experiments in 2D and 3D. We concluded that  $T_1$  is mainly limited by dielectric loss, with loss tangent in agreement with previous fluxonium work. An effective resonator temperature of 70 mK and average thermal photon number  $n_{\text{th}} = 1.2 \times 10^{-2}$  is sufficient to explain the measured  $T_\phi$  in our system. By optimizing the readout line filtering and attenuation, along with reducing  $\chi_{01}/\kappa$ , we predict that the coherence time will grow to the  $2T_1$  limit. Despite the relatively high level of pure dephasing, reaching a single-qubit gate fidelity in excess of 0.999, on par with the state-of-the-art, was possible by using 6 ns pulses. Fast gates that can be tuned in a relatively straightforward manner are a key advantage of fluxonium, where the anharmonicity is about an order of magnitude larger than in transmons. Our results on a fluxonium MCM pave the way to further scaling fluxonium-based quantum processors.

- 
- [1] M. H. Devoret and R. J. Schoelkopf, Superconducting circuits for quantum information: An outlook, *Science* **339**, 1169 (2013).
- [2] M. Kjaergaard, M. E. Schwartz, J. Braumüller, P. Krantz, J. I.-J. Wang, S. Gustavsson, and W. D. Oliver, Superconducting Qubits: Current State of Play, *Annual Review of Condensed Matter Physics* **11**, 369 (2020).
- [3] R. J. Schoelkopf and S. M. Girvin, Wiring up quantum systems, *Nature* **451**, 10.1038/451664a (2008).
- [4] F. Arute, K. Arya, R. Babbush, D. Bacon, J. C. Bardin, R. Barends, R. Biswas, S. Boixo, F. G. Brandao, D. A. Buell, B. Burkett, Y. Chen, Z. Chen, B. Chiaro, R. Collins, W. Courtney, A. Dunsworth, E. Farhi, B. Foxen, A. Fowler, C. Gidney, M. Giustina, R. Graff, K. Guerin, S. Habegger, M. P. Harrigan, M. J. Hartmann, A. Ho, M. Hoffmann, T. Huang, T. S. Humble, S. V. Isakov, E. Jeffrey, Z. Jiang, D. Kafri, K. Kechedzhi, J. Kelly, P. V. Klimov, S. Knysh, A. Korotkov, F. Kostritsa, D. Landhuis, M. Lindmark, E. Lucero, D. Lyakh, S. Mandrà, J. R. McClean, M. McEwen, A. Megrant, X. Mi, K. Michelsen, M. Mohseni, J. Mutus, O. Naaman, M. Neeley, C. Neill, M. Y. Niu, E. Ostby, A. Petukhov, J. C. Platt, C. Quintana, E. G. Rieffel, P. Roushan, N. C. Rubin, D. Sank, K. J. Satzinger, V. Smelyanskiy, K. J. Sung, M. D. Trevithick, A. Vainsencher, B. Villalonga, T. White, Z. J. Yao, P. Yeh, A. Zalcman, H. Neven, and J. M. Martinis, Quantum supremacy using a programmable superconducting processor, *Nature* **574**, 505 (2019).
- [5] E. J. Zhang, S. Srinivasan, N. Sundaresan, D. F. Bogorin, Y. Martin, J. B. Hertzberg, J. Timmerwilke, E. J. Pritchett, J.-B. Yau, C. Wang, W. Landers, E. P. Lewandowski, A. Narasgond, S. Rosenblatt, G. A. Keefe, I. Lauer, M. B. Rothwell, D. T. McClure, O. E. Dial, J. S. Orcutt, M. Brink, and J. M. Chow, High-fidelity superconducting quantum processors via laser-annealing of transmon qubits, *Science Advances* **8** (2022).
- [6] A. G. Fowler, M. Mariantoni, J. M. Martinis, and A. N. Cleland, Surface codes: Towards practical large-scale quantum computation, *Physical Review A - Atomic, Molecular, and Optical Physics* **86**, 10.1103/PhysRevA.86.032324 (2012).
- [7] T. A. Brecht, W. Pfaff, C. Wang, Y. Chu, L. Frunzio, M. H. Devoret, and R. J. Schoelkopf, Multi-layer microwave integrated quantum circuits for scalable quantum computing, *npj Quantum Information* **2**, 10.1038/npjqi.2016.2 (2016).
- [8] R. McDermott, M. G. Vavilov, B. L. Plourde, F. K. Wilhelm, P. J. Liebermann, O. A. Mukhanov, and T. A. Ohki, Quantum-classical interface based on single flux quantum digital logic, *Quantum Science and Technology* **3**, 10.1088/2058-9565/aaa3a0 (2018).
- [9] E. Leonard, M. A. Beck, J. Nelson, B. G. Christensen, T. Thorbeck, C. Howington, A. Opremcak, I. V. Pechenezhskiy, K. Dodge, N. P. Dupuis, M. D. Hutchings, J. Ku, F. Schlenker, J. Suttle, C. Wilen, S. Zhu, M. G. Vavilov, B. L. Plourde, and R. McDermott, Digital Coherent Control of a Superconducting Qubit, *Physical Review Applied* **11**, 10.1103/PhysRevApplied.11.014009

- (2019).
- [10] D. Rosenberg, D. Kim, R. Das, D. Yost, S. Gustavsson, D. Hover, P. Krantz, A. Melville, L. Racz, G. O. Samach, S. J. Weber, F. Yan, J. L. Yoder, A. J. Kerman, and W. D. Oliver, 3D integrated superconducting qubits, *npj Quantum Information* **3**, 10.1038/S41534-017-0044-0 (2017).
  - [11] B. Foxen, J. Y. Mutus, E. Lucero, R. Graff, A. Megrant, Y. Chen, C. Quintana, B. Burkett, J. Kelly, E. Jeffrey, Y. Yang, A. Yu, K. Arya, R. Barends, Z. Chen, B. Chiaro, A. Dunsworth, A. Fowler, C. Gidney, M. Giustina, T. Huang, P. Klimov, M. Neeley, C. Neill, P. Roushan, D. Sank, A. Vainsencher, J. Wenner, T. C. White, and J. M. Martinis, Qubit compatible superconducting interconnects, *Quantum Science and Technology* **3**, 10.1088/2058-9565/aa94fc (2018).
  - [12] A. Dunsworth, R. Barends, Y. Chen, Z. Chen, B. Chiaro, A. Fowler, B. Foxen, E. Jeffrey, J. Kelly, P. V. Klimov, E. Lucero, J. Y. Mutus, M. Neeley, C. Neill, C. Quintana, P. Roushan, D. Sank, A. Vainsencher, J. Wenner, T. C. White, H. Neven, J. M. Martinis, and A. Megrant, A method for building low loss multi-layer wiring for superconducting microwave devices, *Applied Physics Letters* **112**, 10.1063/1.5014033 (2018).
  - [13] D. R. Yost, M. E. Schwartz, J. Mallek, D. Rosenberg, C. Stull, J. L. Yoder, G. Calusine, M. Cook, R. Das, A. L. Day, E. B. Golden, D. K. Kim, A. Melville, B. M. Niedzielski, W. Woods, A. J. Kerman, and W. D. Oliver, Solid-state qubits integrated with superconducting through-silicon vias, *npj Quantum Information* **6**, 10.1038/s41534-020-00289-8 (2020).
  - [14] G. Catelani, R. J. Schoelkopf, M. H. Devoret, and L. I. Glazman, Relaxation and frequency shifts induced by quasiparticles in superconducting qubits, *Phys. Rev. B* **84**, 064517 (2011).
  - [15] L. I. Glazman and G. Catelani, Bogoliubov Quasiparticles in Superconducting Qubits, arXiv:2003.04366 (2020).
  - [16] C.-H. Liu, A. Ballard, D. Olaya, D. R. Schmidt, J. Biesecker, T. Lucas, J. Ullom, S. Patel, O. Rafferty, A. Opremcak, K. Dodge, V. Iaia, T. McBroom, J. L. Dubois, P. F. Hopkins, S. P. Benz, B. L. T. Plourde, and R. McDermott, Single Flux Quantum-Based Digital Control of Superconducting Qubits in a Multi-Chip Module, arXiv:2301.05696 (2023).
  - [17] J. Koch, T. M. Yu, J. Gambetta, A. A. Houck, D. I. Schuster, J. Majer, A. Blais, M. H. Devoret, S. M. Girvin, and R. J. Schoelkopf, Charge-insensitive qubit design derived from the Cooper pair box, *Physical Review A - Atomic, Molecular, and Optical Physics* **76**, 10.1103/PhysRevA.76.042319 (2007).
  - [18] J. Q. You, X. Hu, S. Ashhab, and F. Nori, Low-decoherence flux qubit, *Physical Review B - Condensed Matter and Materials Physics* **75**, 10.1103/PhysRevB.75.140515 (2007).
  - [19] M. Steffen, S. Kumar, D. P. Divincenzo, J. R. Rozen, G. A. Keefe, M. B. Rothwell, and M. B. Ketchen, High-coherence hybrid superconducting qubit, *Physical Review Letters* **105**, 10.1103/PhysRevLett.105.100502 (2010).
  - [20] X. Li, Y. Zhang, C. Yang, Z. Li, J. Wang, T. Su, M. Chen, Y. Li, C. Li, Z. Mi, X. Liang, C. Wang, Z. Yang, Y. Feng, K. Linghu, H. Xu, J. Han, W. Liu, P. Zhao, T. Ma, R. Wang, J. Zhang, Y. Song, P. Liu, Z. Wang, Z. Yang, G. Xue, Y. Jin, and H. Yu, Vacuum-gap transmon qubits realized using flip-chip technology, *Applied Physics Letters* **119**, 10.1063/5.0068255 (2021).
  - [21] S. Kosen, H.-X. Li, M. Rommel, D. Shiri, C. Warren, L. Grönberg, J. Salonen, T. Abad, J. Biznárová, M. Caputo, L. Chen, K. Grigoras, G. Johansson, A. F. Kockum, C. Križan, D. P. Lozano, G. Norris, A. Osman, J. Fernández-Pendás, A. Ronzani, A. F. Roudsari, S. Simbierowicz, G. Tancredi, A. Wallraff, C. Eichler, J. Govenius, and J. Bylander, Building Blocks of a Flip-Chip Integrated Superconducting Quantum Processor, *Quantum Science and Technology* **7**, 10.1088/2058-9565/ac734b (2022).
  - [22] P. Jurcevic, A. Javadi-Abhari, L. S. Bishop, I. Lauer, D. F. Bogorin, M. Brink, L. Capelluto, O. Günlük, T. Itoko, N. Kanazawa, A. Kandala, G. A. Keefe, K. Kruschelich, W. Landers, E. P. Lewandowski, D. T. McClure, G. Nannicini, A. Narasgond, H. M. Nayfeh, E. Pritchett, M. B. Rothwell, S. Srinivasan, N. Sundaresan, C. Wang, K. X. Wei, C. J. Wood, J. B. Yau, E. J. Zhang, O. E. Dial, J. M. Chow, and J. M. Gambetta, Demonstration of quantum volume 64 on a superconducting quantum computing system, *Quantum Sci. Technol.* **6**, 025020 (2021).
  - [23] A. Gold, J. P. Paquette, A. Stockklauser, M. J. Reagor, M. S. Alam, A. Bestwick, N. Didier, A. Nersisyan, F. Oruc, A. Razavi, B. Scharmann, E. A. Sete, B. Sur, D. Venturelli, C. J. Winkleblack, F. Wudarski, M. Harburn, and C. Rigetti, Entanglement across separate silicon dies in a modular superconducting qubit device, *npj Quantum Information* **7**, 10.1038/s41534-021-00484-1 (2021).
  - [24] V. E. Manucharyan, J. Koch, L. I. Glazman, and M. H. Devoret, Fluxonium: Single cooper-pair circuit free of charge offsets, *Science* **326**, 113 (2009).
  - [25] L. B. Nguyen, Y. H. Lin, A. Somoroff, R. Mencia, N. Grabon, and V. E. Manucharyan, High-Coherence Fluxonium Qubit, *Physical Review X* **9**, 041041 (2019).
  - [26] A. Somoroff, Q. Ficheux, R. A. Mencia, H. Xiong, R. Kuzmin, and V. Manucharyan, Millisecond Coherence in a Superconducting Qubit, arXiv:2103.08578 (2021).
  - [27] Z. Chen, J. Kelly, C. Quintana, R. Barends, B. Campbell, Y. Chen, B. Chiaro, A. Dunsworth, A. G. Fowler, E. Lucero, E. Jeffrey, A. Megrant, J. Mutus, M. Neeley, C. Neill, P. J. O'Malley, P. Roushan, D. Sank, A. Vainsencher, J. Wenner, T. C. White, A. N. Korotkov, and J. M. Martinis, Measuring and Suppressing Quantum State Leakage in a Superconducting Qubit, *Physical Review Letters* **116**, 10.1103/PhysRevLett.116.020501 (2016).
  - [28] Q. Ficheux, L. B. Nguyen, A. Somoroff, H. Xiong, K. N. Nesterov, M. G. Vavilov, and V. E. Manucharyan, Fast Logic with Slow Qubits: Microwave-Activated Controlled-Z Gate on Low-Frequency Fluxoniums, *Physical Review X* **11**, 021026 (2021).
  - [29] H. Xiong, Q. Ficheux, A. Somoroff, L. B. Nguyen, E. Dogan, D. Rosenstock, C. Wang, K. N. Nesterov, M. G. Vavilov, and V. E. Manucharyan, Arbitrary controlled-phase gate on fluxonium qubits using differential ac-Stark shifts, arXiv:2103.04491 (2021).
  - [30] E. Dogan, D. Rosenstock, L. L. Guevel, H. Xiong, R. A. Mencia, A. Somoroff, K. N. Nesterov, M. G. Vavilov, V. E. Manucharyan, and C. Wang, Demonstration of the Two-Fluxonium Cross-Resonance Gate, arXiv:2204.11829 (2022).

- [31] I. N. Moskalenko, I. A. Simakov, N. N. Abramov, A. A. Grigorev, D. O. Moskalev, A. A. Pishchimova, N. S. Smirnov, E. V. Zikiy, I. A. Rodionov, and I. S. Besedin, High fidelity two-qubit gates on fluxoniums using a tunable coupler, *npj Quantum Information* **8**, 10.1038/s41534-022-00644-x (2022).
- [32] F. Bao, H. Deng, D. Ding, R. Gao, X. Gao, C. Huang, X. Jiang, H.-S. Ku, Z. Li, X. Ma, X. Ni, J. Qin, Z. Song, H. Sun, C. Tang, T. Wang, F. Wu, T. Xia, W. Yu, F. Zhang, G. Zhang, X. Zhang, J. Zhou, X. Zhu, Y. Shi, J. Chen, H.-H. Zhao, and C. Deng, Fluxonium: an alternative qubit platform for high-fidelity operations, *Physical Review Letters* **129**, 10.1103/PhysRevLett.129.010502 (2021).
- [33] L. B. Nguyen, G. Koolstra, Y. Kim, A. Morvan, T. Chistolini, S. Singh, K. N. Nesterov, C. Jünger, L. Chen, Z. Pedramrazi, B. K. Mitchell, J. M. Kreikebaum, S. Puri, D. I. Santiago, and I. Siddiqi, Scalable High-Performance Fluxonium Quantum Processor, *PRX Quantum* **3**, 10.1103/PRXQuantum.3.037001 (2022).
- [34] H. Zhang, S. Chakram, T. Roy, N. Earnest, Y. Lu, Z. Huang, D. K. Weiss, J. Koch, and D. I. Schuster, Universal Fast-Flux Control of a Coherent, Low-Frequency Qubit, *Physical Review X* **11**, 011010 (2021).
- [35] M. Göppel, A. Fragner, M. Baur, R. Bianchetti, S. Filipp, J. M. Fink, P. J. Leek, G. Puebla, L. Steffen, and A. Wallraff, Coplanar waveguide resonators for circuit quantum electrodynamics, *Journal of Applied Physics* **104**, 10.1063/1.3010859 (2008).
- [36] A. Wallraff, D. I. Schuster, A. Blais, L. Frunzio, R. S. Huang, J. Majer, S. Kumar, S. M. Girvin, and R. J. Schoelkopf, Strong coupling of a single photon to a superconducting qubit using circuit quantum electrodynamics, *Nature* **431** (2004).
- [37] A. Blais, R.-S. Huang, A. Wallraff, S. M. Girvin, and R. J. Schoelkopf, Cavity quantum electrodynamics for superconducting electrical circuits: An architecture for quantum computation, *Physical Review A* **69**, 062320 (2004).
- [38] C. Wang, C. Axline, Y. Y. Gao, T. Brecht, Y. Chu, L. Frunzio, M. H. Devoret, and R. J. Schoelkopf, Surface participation and dielectric loss in superconducting qubits, *Applied Physics Letters* **107**, 162601 (2015).
- [39] A. P. Place, L. V. Rodgers, P. Mundada, B. M. Smitham, M. Fitzpatrick, Z. Leng, A. Premkumar, J. Bryon, S. Sussman, G. Cheng, T. Madhavan, H. K. Babla, B. Jäck, A. Gyenis, N. Yao, R. J. Cava, N. P. de Leon, and A. A. Houck, New material platform for superconducting transmon qubits with coherence times exceeding 0.3 milliseconds, *Nature Communications* **12**, 1779 (2021).
- [40] E. Hahn, Spin Echoes, *Physical Review* **80** (1950).
- [41] J. M. Martinis, S. Nam, J. Aumentado, K. M. Lang, and C. Urbina, Decoherence of a superconducting qubit due to bias noise, *Physical Review B - Condensed Matter and Materials Physics* **67**, 10.1103/PhysRevB.67.094510 (2003).
- [42] S. Meiboom and D. Gill, Modified spin-echo method for measuring nuclear relaxation times, *Review of Scientific Instruments* **29**, 10.1063/1.1716296 (1958).
- [43] J. Bylander, S. Gustavsson, F. Yan, F. Yoshihara, K. Harrabi, G. Fitch, D. G. Cory, Y. Nakamura, J. S. Tsai, and W. D. Oliver, Noise spectroscopy through dynamical decoupling with a superconducting flux qubit, *Nature Physics* **7**, 10.1038/nphys1994 (2011).
- [44] F. Yoshihara, K. Harrabi, A. O. Niskanen, Y. Nakamura, and J. S. Tsai, Decoherence of flux qubits due to 1/f flux noise, *Physical Review Letters* **97**, 10.1103/PhysRevLett.97.167001 (2006).
- [45] P. Kumar, S. Sendelbach, M. A. Beck, J. W. Freeland, Z. Wang, H. Wang, C. C. Yu, R. Q. Wu, D. P. Pappas, and R. McDermott, Origin and Reduction of 1 / f Magnetic Flux Noise in Superconducting Devices, *Physical Review Applied* **6**, 10.1103/PhysRevApplied.6.041001 (2016).
- [46] P. Bertet, I. Chiorescu, G. Burkard, K. Semba, C. J. Harmans, D. P. Divincenzo, and J. E. Mooij, Dephasing of a superconducting qubit induced by photon noise, *Physical Review Letters* **95**, 10.1103/PhysRevLett.95.257002 (2005).
- [47] Z. Wang, S. Shankar, Z. K. Minev, P. Campagne-Ibarcq, A. Narla, and M. H. Devoret, Cavity Attenuators for Superconducting Qubits, *Physical Review Applied* **11**, 014031 (2019).
- [48] F. Yan, S. Gustavsson, A. Kamal, J. Birenbaum, A. P. Sears, D. Hover, T. J. Gudmundsen, D. Rosenberg, G. Samach, S. Weber, J. L. Yoder, T. P. Orlando, J. Clarke, A. J. Kerman, and W. D. Oliver, The flux qubit revisited to enhance coherence and reproducibility, *Nature Communications* **7**, 12964 (2016).
- [49] J. H. Yeh, J. Lefebvre, S. Premaratne, F. C. Wellstood, and B. S. Palmer, Microwave attenuators for use with quantum devices below 100 mK, *Journal of Applied Physics* **121**, 224501 (2017).
- [50] J. Gambetta, A. Blais, D. I. Schuster, A. Wallraff, L. Frunzio, J. Majer, M. H. Devoret, S. M. Girvin, and R. J. Schoelkopf, Qubit-photon interactions in a cavity: Measurement-induced dephasing and number splitting, *Physical Review A - Atomic, Molecular, and Optical Physics* **74**, 10.1103/PhysRevA.74.042318 (2006).
- [51] D. I. Schuster, A. A. Houck, J. A. Schreier, A. Wallraff, J. M. Gambetta, A. Blais, L. Frunzio, J. Majer, B. Johnson, M. H. Devoret, S. M. Girvin, and R. J. Schoelkopf, Resolving photon number states in a superconducting circuit, *Nature* **445**, 10.1038/nature05461 (2007).
- [52] E. Magesan, J. M. Gambetta, and J. Emerson, Scalable and robust randomized benchmarking of quantum processes, *Physical Review Letters* **106**, 180504 (2011).
- [53] E. Magesan, J. M. Gambetta, B. R. Johnson, C. A. Ryan, J. M. Chow, S. T. Merkel, M. P. Da Silva, G. A. Keefe, M. B. Rothwell, T. A. Ohki, M. B. Ketchen, and M. Steffen, Efficient measurement of quantum gate error by interleaved randomized benchmarking, *Physical Review Letters* **109** (2012).

**Supplemental Material for  
‘Flip-Chip Packaging of Fluxonium Qubits’**

A. Somoroff et al.  
(Dated: March 3, 2023)

This document contains (6 pages total):

8 Supplementary Notes  
4 Supplementary Figures  
2 Supplementary Tables

### Supplementary Note 1: Device Parameters

The bare fluxonium Hamiltonian reads [1]:

$$\hat{H}_{\text{fl}} = 4E_C \hat{n}^2 + \frac{1}{2} E_L \hat{\varphi}^2 - E_J \cos \left( \hat{\varphi} - 2\pi \frac{\Phi_{\text{ext}}}{\Phi_0} \right). \quad (\text{S1})$$

Additionally, the resonator at frequency  $\omega_r$  has Hamiltonian:

$$\hat{H}_{\text{r}} = \hbar \omega_r (\hat{a}^\dagger \hat{a} + 1/2) \quad (\text{S2})$$

and the Hamiltonian term for fluxonium-resonator coupling in the dispersive regime is given by:

$$\hat{H}_{\text{c}} = -\hbar g \hat{n} (\hat{a}^\dagger + \hat{a}) \quad (\text{S3})$$

where  $g$  is the fluxonium-resonator coupling rate. The spectroscopy data in Figure 2 in the main text are fit to the numerical diagonalization of Hamiltonian:

$$\hat{H} = \hat{H}_{\text{fl}} + \hat{H}_{\text{r}} + \hat{H}_{\text{c}} \quad (\text{S4})$$

in the LC oscillator basis. A Hilbert space of 25 fluxonium levels and 5 resonator levels was used.

### Supplementary Note 2: Qubit Parameter Summary

We extensively characterized fluxoniums 3 and 4, and have summarized their main parameters in the table below. For coherence times, we report the maximum values measured during the device cooldown as well as the mean values taken from interleaved loops. Unless otherwise specified, the parameter values are taken at the sweet spot  $\Phi_{\text{ext}}/\Phi_0 = 0.5$ .

Fluxonium	3	4
$E_J/h$ (GHz)	2.50	2.36
$E_L/h$ (GHz)	1.14	1.14
$E_C/h$ (GHz)	0.89	0.89
$\omega_{01}/2\pi$ (GHz)	1.252	1.330
$\omega_{12}/\omega_{01}$	2.14	1.99
$T_1^{\max}$ ( $\mu\text{s}$ )	77	58
$T_2^{E,\max}$ ( $\mu\text{s}$ )	38	33
$\langle T_1 \rangle$ ( $\mu\text{s}$ )	55.1	33.6
$\langle T_2^E \rangle$ ( $\mu\text{s}$ )	27.5	23.2
$T_\phi$ ( $\mu\text{s}$ )	36.6	35.4
$\omega_r/2\pi$ (GHz)	6.4493	6.1391
$g/2\pi$ (MHz)	86	85
$\chi_{01}/2\pi$ (MHz)	1.39	0.63
$\kappa/2\pi$ (MHz)	0.391	0.269
$\tan \delta_C (\times 10^{-6})$	1.6	2.0

Supplementary Table 1. Summary of qubit parameters for each fluxonium under study at half flux quantum.

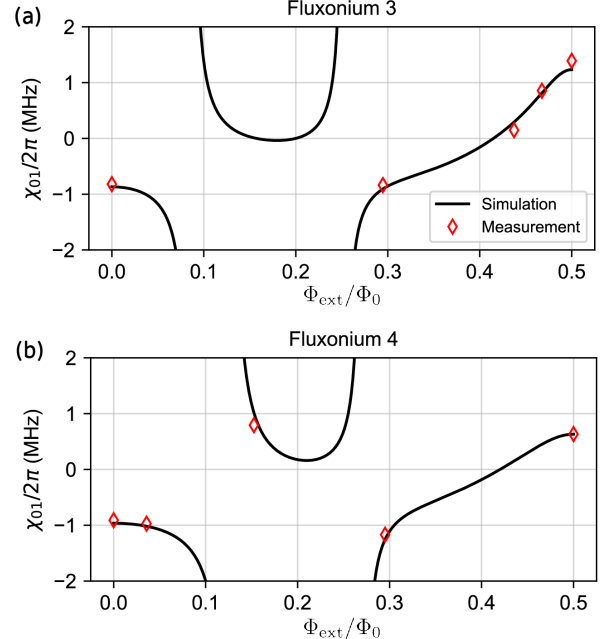
### Supplementary Note 3: Readout

#### A. Qubit-Resonator Interaction

The fluxonium circuits are capacitively coupled to a  $\lambda/4$  CPW resonator, which is housed separately on the carrier chip. The fluxonium-resonator coupling rate  $g$  is found empirically from the spectroscopy data in Figure 2 in the main text. The pull on the resonator frequency due to bare fluxonium state  $|j\rangle$ , known as the dispersive shift of state  $|j\rangle$ , is given by [2]:

$$\chi_j = g^2 \sum_k |\hat{n}_{jk}|^2 \frac{2\omega_{jk}}{\omega_{jk}^2 - \omega_r^2}, \quad (\text{S5})$$

where  $\hat{n}_{jk}$  is the fluxonium charge matrix element between states  $|j\rangle$  and  $|k\rangle$  in units of Cooper pairs. The dispersive shift of the transition between states  $|i\rangle$  and  $|j\rangle$  is then  $\chi_{ij} = \chi_i - \chi_j$ . Crucially, equation S5 shows that the qubit transition can have a large dispersive shift due to the contributions of the higher levels where  $\omega_{jk} \simeq \omega_r$ , despite the large detuning between  $\omega_{01}$  and  $\omega_r$ . Supplementary Figure 1 uses equation S5 to plot  $\chi_{01}$  across half a flux period for fluxoniums 3 and 4. Red diamonds are measured  $\chi_{01}$  at various external flux biases, showing excellent agreement between theory and experiment. The simulation uses 25 fluxonium levels, 20 of which are used in the summation to find  $\chi_{01}$ .



Supplementary Figure 1. Simulated qubit dispersive shift  $\chi_{01}$  for fluxoniums 3 (a) and 4 (b) using equation S5 and the parameters in table 1. We include measured values of  $\chi_{01}$  at various external flux biases.

In our system, the fluxonium-resonator coupling rate  $g$  in equations S3 and S5 is given by:

$$g = \frac{1}{2} \frac{C_{qr}}{C_\Sigma C_r} \frac{1}{\sqrt{\zeta_q \zeta_r}} \quad (\text{S6})$$

where  $\zeta_q = \frac{R_q}{2\pi} \sqrt{\frac{8E_C}{E_L+E_J}}$  and  $\zeta_r = \sqrt{\frac{L_r}{C_r}}$  are the fluxonium and resonator characteristic impedances, respectively.  $R_q = h/(2e)^2$  is the resistance quantum.

## B. Thermal Photon Dephasing

The qubit dephasing rate due to thermal photons in the cavity is given by:

$$\Gamma_\phi^{\text{th}} = \frac{n_{\text{th}} \kappa \chi_{01}^2}{\kappa^2 + \chi_{01}^2} \quad (\text{S7})$$

in the low photon number  $n_{\text{th}}$  limit [3, 4]. Plugging in the values of  $\kappa$ ,  $\chi_{01}$ , and  $T_\phi$  for each fluxonium (see Supplementary Note 2), we find the average thermal photon numbers  $n_{\text{th}} = (1.2 \pm 0.1) \times 10^{-2}$  and  $(2.0 \pm 0.2) \times 10^{-2}$  for fluxonions 3 and 4, respectively. These values correspond to resonator temperatures of  $70 \pm 1$  mK and  $75 \pm 2$  mK for fluxonions 3 and 4, respectively.

## Supplementary Note 4: Dielectric Loss

In terms of the charge matrix element  $\hat{n}_{ij}$ , the decay rate between eigenstates  $|i\rangle$ ,  $|j\rangle$  due to dielectric loss at a finite temperature  $T$  reads:

$$\Gamma_{ij}^{\text{diel}} = \frac{16\pi E_C}{h} |\hat{n}_{ij}|^2 \tan \delta_C \left[ (1 + \coth \left( \frac{\hbar \omega_{ij}}{2k_B T} \right)) \right] \quad (\text{S8})$$

where  $\tan \delta_C$  is the effective dielectric loss tangent of the total capacitance  $C_\Sigma$  of fluxonium (note that:  $C_\Sigma = e^2/2E_C$ ). We used this expression to calculate corresponding loss tangents for fluxonions 3 and 4, given their maximal  $T_1$  values at the sweet spot. We assume a qubit temperature of  $T = 20$  mK. Since  $\tan \delta_C$  can depend weakly on frequency, the reported values for fluxonions 3 and 4 should be interpreted as the value at their qubit frequencies (see Supplementary Table 1).

## Supplementary Note 5: Coherence Analysis

### A. 1/f Flux Noise

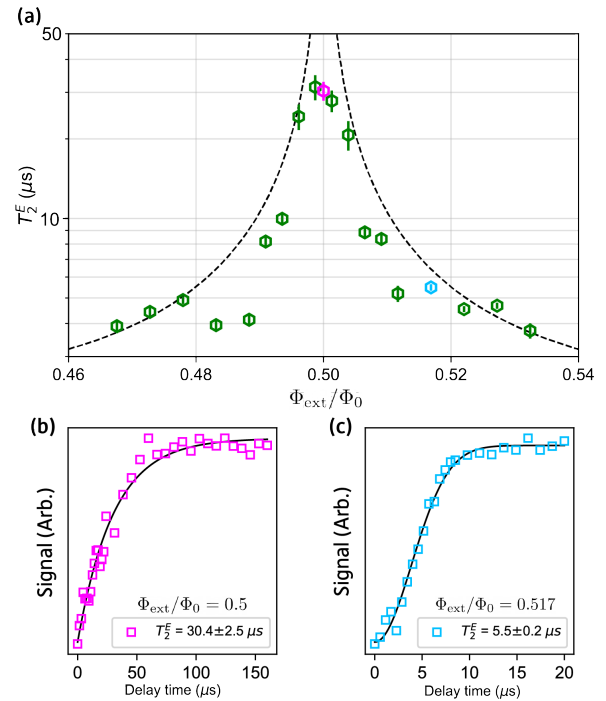
$1/f$  flux noise is known to be a leading cause of pure dephasing in flux-sensitive qubits, with a noise spectral density given by [5–9]:

$$S_\Phi(\omega) = 2\pi \frac{A_\Phi^2}{\omega}, \quad (\text{S9})$$

where  $A_\Phi$  is the flux noise amplitude at 1 Hz. The dephasing rate due to first-order  $1/f$  flux noise is given by:

$$\Gamma_\Phi = A_\Phi \sqrt{\ln 2} \frac{\partial \omega}{\partial \Phi_{\text{ext}}}. \quad (\text{S10})$$

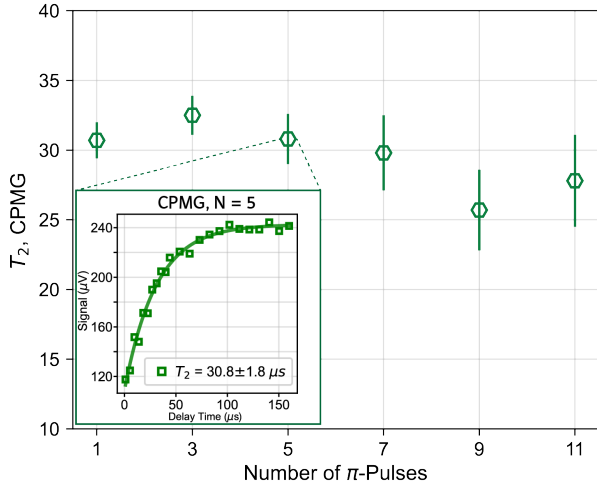
This leads to a  $T_2^E$  measurement signal decaying with a Gaussian envelope, with decay constant  $T_\phi^\Phi = 1/\Gamma_\Phi$ . This is the case when fluxonium is flux biased off of the sweet spot. On the sweet spot, the first-order sensitivity to  $1/f$  flux noise vanishes, and we observe an exponentially decaying echo signal [10]. To determine  $A_\Phi$  in our experimental setup, we measured  $T_2^E$  at various  $\Phi_{\text{ext}}$  in fluxonium 3 (see Supplementary Figure 2). The observed dependence of  $T_2^E$  versus external flux bias corresponds to  $A_\Phi = 5.5 \mu\Phi_0/\sqrt{\text{Hz}}$ , in agreement with the previously cited work.



Supplementary Figure 2. (a)  $T_2^E$  versus external magnetic flux  $\Phi_{\text{ext}}$ . The data are fit to a decaying Gaussian function off sweet spot and to a decaying exponential at the sweet spot. Dashed black curve represents the simulated values for first-order flux noise-induced dephasing time  $T_\phi^\Phi$  for flux noise amplitude  $A_\Phi = 5.5 \mu\Phi_0/\sqrt{\text{Hz}}$  at 1 Hz. At the sweet spot, the first-order limit diverges, and coherence is mainly limited by energy relaxation and uncorrelated (white) noise. (b) Measurement trace at the sweet spot. The data are fit to a decaying exponential and the decay constant corresponds to the magenta point in (a). (c) Measurement trace at a flux bias point off the sweet spot. The data are fit to decaying Gaussian and the decay constant corresponds to the blue point in (a).

## B. CPMG

By increasing the number of refocusing  $\pi$ -pulses  $N$  in a Hahn-Echo sequence (where  $N = 1$ ), the qubit will be more sensitive to noise at successively higher frequencies [5, 11]. This is known as a Carr-Purcell-Meiboom-Gill (CPMG) sequence [12], where the additional refocusing  $\pi$ -pulses act as a bandpass filter centered at a frequency determined by  $N$  and the free evolution time [9, 13]. If the noise spectrum is white within the region we sweep our filter, we expect the measured decay time to remain constant with an increasing number of  $\pi$ -pulses. If the noise spectral density  $\propto 1/f$ , we expect  $T_2$  to rise for  $N > 1$ .



Supplementary Figure 3. CPMG experiment where we sweep the number of refocusing  $\pi$ -pulses  $N$  from 1 to 11. The resulting measurement traces are then fitted to a decaying exponential function and the decay constant is plotted. We find that there is no significant correlation between number of pulses and  $T_2$  in this range. Inset shows the measurement trace and fit for 5 intermediate  $\pi$ -pulses.

## Supplementary Note 6: Qubit Gates

### A. Microwave Pulses

The  $X/2$  and  $Y/2$  pulses were synthesized with a Keysight M3202 AWG and a Rohde & Schwarz SGS100A Vector Modulation RF source for low frequency IQ modulation. We used cosine-envelope pulses with an envelope function:

$$f(t) = \frac{\epsilon}{2}[1 - \cos(2\pi t/t_g)], \quad (\text{S11})$$

where  $\epsilon$  is the drive amplitude and  $t_g$  is the total gate duration. We set  $t_g = 6$  ns in our experiments. The

cosine envelope is chosen over Gaussian to avoid truncation at the edges. The  $X$  ( $Y$ ) pulses consist of pairs of concatenated  $X/2$  ( $Y/2$ ) pulses. To determine the individual gate fidelities we performed interleaved randomized benchmarking [14], the results of which are shown in Supplementary Table 2.

We tuned the qubit drive frequency  $\omega_d$  by taking Ramsey measurements with varying  $\omega_d$ . After obtaining the  $\omega_d = \omega_{01}$ , we performed a pulse train measurement to determine the optimal pulse amplitude. The pulse train consisted of sweeping the amplitude for a train of 4, 16, 36, 64, 100, and 144 pulses. The resulting trace of each measurement is effectively a Rabi oscillation, where the Rabi frequency increases with the number of pulses in the train. The amplitude corresponding to the same phase in the Rabi oscillations across all the trains is the optimal  $X/2$ -pulse amplitude. After performing initial randomized benchmarking experiments, the pulse amplitude was further fine-tuned using the ORBIT procedure [15].

Gate	X	$X/2$	$-X/2$	Y	$Y/2$	$-Y/2$
$1 - F_g (\times 10^{-4})$	8.1	3.1	2.6	6.1	2.1	5.9

Supplementary Table 2. Gate error rates  $1 - F_g$  of each Clifford-generating gate obtained from interleaved randomized benchmarking for fluxonium 3. The relative error of each error rate is approximately 10%.

## B. Gate Simulation

The simulation results shown in Figure 4b in the main text were obtained as follows. We truncated the fluxonium and transmon Hamiltonians to only consider the lowest three eigenstates. We then define a pulse with driving frequency  $\omega_d = \omega_{01}$ , and envelope given by equation (S11). At each gate duration  $t_g$ , we find the pulse amplitude that maximizes the probability of being in state  $|1\rangle$  after applying it to state  $|0\rangle$ . In our case, we define the error rate as the level of leakage to the second excited state  $|2\rangle$ , which increases as the pulse amplitude increases with shorter gate duration.

## Supplementary Note 7: Fabrication

### A. Quantum Chip

We fabricated the device on a high resistivity silicon substrate. *Cleaning:* The chip is prepared by sonicating it in acetone, then isopropyl alcohol (IPA) for 3 minutes each. *Electron Beam Resist Application:* 1 drop of MMA EL-13 electron beam resist is applied to the chip, then spun at 5000 RPM for 1 minute. The resist is then baked on a hotplate for 1 minute at 180°C. A second layer of resist is then applied: 1 drop of 950 PMMA A3 electron beam resist spun at 4000 RPM for 1 minute before

baking at 180°C for 30 minutes. *Electron Beam Lithography:* The circuit is written with a 100 kV Elionix Electron Beam Lithography system, using a beam current of 1 nA. *Resist Development:* Mask is developed for 2 minutes in a 3:1 IPA:DI solution at 6°C. The chip is lightly shaken back and forth by hand at around 1-2 Hz while in the developer. *Metal Deposition:* Chip is loaded into a Plassys deposition system and the loadlock is pumped on for 20 hours until the pressure reaches  $1.3 \times 10^{-7}$  mBar prior to deposition. The deposition is comprised of the following steps: 1. 20 second Ar etch at each deposition angle ( $\pm 23.83^\circ$ ) 2. Deposit Ti into the chamber at 0.1 nm/s for 2 minutes 3. First Al deposition: 20 nm is deposited at 1 nm/s at an angle of  $23.83^\circ$  4. 10 minutes of oxidation at 100 mBar 5. Second Al deposition: 40 nm is deposited at 1 nm/s at an angle of  $-23.83^\circ$  6. 20 minutes of oxidation at 10 mBar (capping). *Resist Lift-off:* Chip is bathed in acetone for 3 hours at 60°C. Then it is sonicated in the acetone for 5 seconds, followed by 10 seconds of sonication in IPA. Finally, chip is blown dry with  $N_2$ .

### B. Carrier Chip

The process is based on SEEQC's two-niobium-superconducting-layers recipe for quantum applications (seeqc.com/chip-foundry-services). The process involves substrate preparation, niobium (Nb) sputtering, plasma enhanced chemical vapor deposition (PECVD) of  $\text{SiO}_2/\text{SiN}_x$ , chemical mechanical polishing (CMP), photolithography, and dry etching. The substrate is a high resistivity 6" Si wafer. It is first cleaned by spin scrubbing with acetone and spin rinse drying with IPA. Then the native oxide on the wafer is removed by BOE prior to loading into the deposition chamber. Once the chamber reaches a base pressure of  $1.3 \times 10^{-7}$  mBar, Nb is deposited by DC sputtering with target thickness 200 nm. The coplanar microstrip lines, feedthroughs, resonators, and qubit control lines are then patterned in this layer. All the patterning for this process is done using a maskless laser writer capable of resolving 600 nm features with an i-line resist process. Then the Nb is inductively coupled plasma (ICP) etched in chlorine chemistry optimized for good selectivity to silicon. Moreover, an endpoint detection was implemented to minimize the overetch into the substrate and to keep the overetch to within 10 nm. Next, the resist is stripped in an acetone sonicating bath, followed by 600 nm of low loss PECVD  $\text{SiN}_x$  deposited with CMP to planarize the layer. The wafer is then coated with PECVD  $\text{SiO}_2$  of thickness 150 nm for an inter-layer dielectric. The vias to the bottom Nb layer are then patterned and dry etched, which opens access to the wiring, grounds, bump and contact pad connections. Then a second Nb layer of thickness 300 nm is deposited, followed by patterning of the wiring, ground straps, and contacts.

The Nb is then dry etched in reactive ion etcher (RIE); at this step the exposed dielectric is completely dry etched from the wafer to minimize the dielectric participation ratio. After this step, there is only dielectric remaining under the wiring and ground straps. Next, the contact pads are patterned: trilayer Mo/Pd/Au of thickness 40 nm/100 nm/200 nm is deposited and lifted off. Finally, the bump layer is patterned: Al/In of thickness 5  $\mu\text{m}$ /1  $\mu\text{m}$  is deposited and lifted off. The carrier chips of size  $10 \times 10 \text{ mm}^2$  are then diced out and ready for flip-chip bonding.

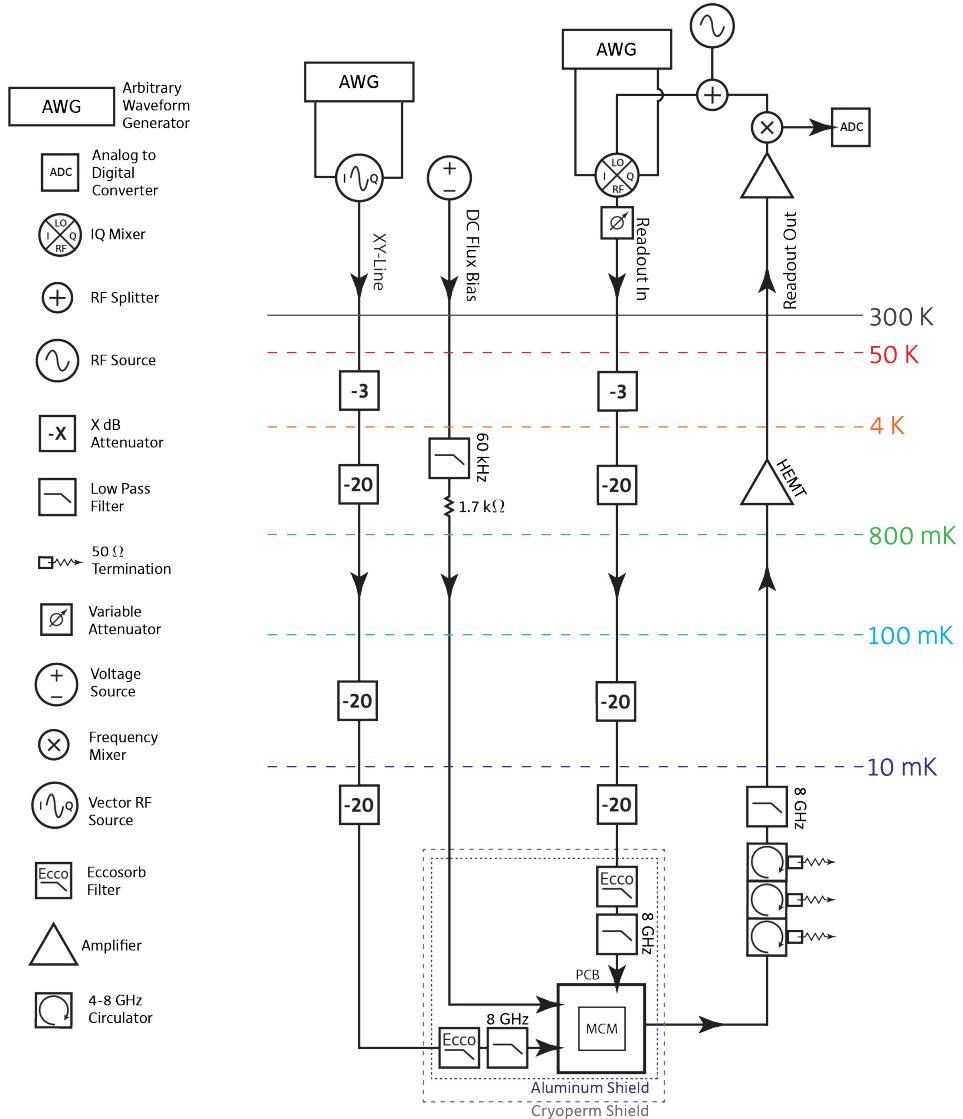
### C. Multi-Chip Module (MCM)

The multi-chip module was assembled using a Karl Suss / Microtec FC 150 Flip Chip Bonder. The tool holds the chip and carrier on two vacuum chucks while adjusting the relative position of alignment marks viewed through a two-objective microscope assembly. The bonder was calibrated immediately before MCM assembly, such that the lateral misalignment between chip and carrier is within 1  $\mu\text{m}$ . The chip and carrier are aligned parallel to within 25  $\mu\text{rad}$ .

The MCM was assembled by a cold compression process with a force of  $294 \text{ N/mm}^2$ , held constant for 2 minutes. Distributed over the 152 square bumps, each 120  $\mu\text{m}$  wide (8.8% of the total flip-chip area), this force is equivalent to 197 grams per bump. Post-bond measurement of bump height on other MCMs has indicated that this force compresses the top 1  $\mu\text{m}$  layer of indium slightly, but does not significantly compress the underlying aluminum bump, such that the aluminum acts as a hard stop to control inter-chip spacing. After bonding, a small amount of low-temperature microelectronic-compatible epoxy was applied to the corners of the chip, away from critical circuit components, to maintain integrity of the MCM during sample handling and installation.

### Supplementary Note 8: Experimental Setup

The experiment was performed in a BlueFors LD400 dilution refrigerator (DR) with a base temperature  $\sim 8 \text{ mK}$ . The driving and readout lines are heavily attenuated and filtered as depicted in Supplementary Figure 4. Note that no special filtering was used in the readout line and no radiation-absorbing coating was used inside the refrigerator. The MCM was mounted and wirebonded to a printed circuit board (PCB), which in turn was housed in a copper package. This package was bolted to a coldfinger extending from the 10 mK stage of the DR. The device package was encased in a superconducting (aluminum) shield as well as a cryoperm shield. Additionally, we used a room-temperature magnetic shield inside the outer vacuum can of the refrigerator.



Supplementary Figure 4. Schematic of the wiring of the refrigerator and room temperature setup. The XY-line and readout input line are heavily attenuated and filtered using 63 dB of commercial attenuators (BlueFors cryogenic attenuators) along with K&L low-pass filters, and eccosorb low pass filters (manufactured by BlueFors). The DC flux bias line consists of a twisted pair, the positive terminal set by a voltage source and the negative terminal connected to the common ground plane of the chip.

- 
- [1] V. E. Manucharyan, J. Koch, L. I. Glazman, and M. H. Devoret, Fluxonium: Single cooper-pair circuit free of charge offsets, *Science* **326**, 113 (2009).
- [2] Y.-H. Lin, L. B. Nguyen, N. Grabon, J. San Miguel, N. Pankratova, and V. E. Manucharyan, Demonstration of Protection of a Superconducting Qubit from Energy Decay, *Physical Review Letters* **120**, 150503 (2018).
- [3] A. A. Clerk and D. W. Utami, Using a qubit to measure photon-number statistics of a driven thermal oscillator, *Physical Review A - Atomic, Molecular, and Optical Physics* **75**, 10.1103/PhysRevA.75.042302 (2007).
- [4] Z. Wang, S. Shankar, Z. K. Minev, P. Campagne-Ibarcq, A. Narla, and M. H. Devoret, Cavity Attenuators for Superconducting Qubits, *Physical Review Applied* **11**, 014031 (2019).
- [5] J. M. Martinis, S. Nam, J. Aumentado, K. M. Lang, and C. Urbina, Decoherence of a superconducting qubit due to bias noise, *Physical Review B - Condensed Matter and Materials Physics* **67**, 10.1103/PhysRevB.67.094510 (2003).
- [6] F. Yoshihara, K. Harrabi, A. O. Niskanen, Y. Nakamura, and J. S. Tsai, Decoherence of flux qubits due to 1/f flux noise, *Physical Review Letters* **97**, 10.1103/Phys-

- RevLett.97.167001 (2006).
- [7] R. H. Koch, D. P. Divincenzo, and J. Clarke, Model for 1/f flux noise in SQUIDs and qubits, Physical Review Letters **98**, 10.1103/PhysRevLett.98.267003 (2007).
  - [8] P. Kumar, S. Sendelbach, M. A. Beck, J. W. Freeland, Z. Wang, H. Wang, C. C. Yu, R. Q. Wu, D. P. Pappas, and R. McDermott, Origin and Reduction of 1 /f Magnetic Flux Noise in Superconducting Devices, Physical Review Applied **6**, 10.1103/PhysRevApplied.6.041001 (2016).
  - [9] F. Yan, S. Gustavsson, A. Kamal, J. Birenbaum, A. P. Sears, D. Hover, T. J. Gudmundsen, D. Rosenberg, G. Samach, S. Weber, J. L. Yoder, T. P. Orlando, J. Clarke, A. J. Kerman, and W. D. Oliver, The flux qubit revisited to enhance coherence and reproducibility, Nature Communications **7**, 12964 (2016).
  - [10] L. B. Nguyen, Y. H. Lin, A. Somoroff, R. Mencia, N. Grabon, and V. E. Manucharyan, High-Coherence Fluxonium Qubit, Physical Review X **9**, 041041 (2019).
  - [11] Å. Cywiński, R. M. Lutchyn, C. P. Nave, and S. Das Sarma, How to enhance dephasing time in superconducting qubits, Physical Review B - Condensed Matter and Materials Physics **77**, 10.1103/PhysRevB.77.174509 (2008).
  - [12] S. Meiboom and D. Gill, Modified spin-echo method for measuring nuclear relaxation times, Review of Scientific Instruments **29**, 10.1063/1.1716296 (1958).
  - [13] J. Bylander, S. Gustavsson, F. Yan, F. Yoshihara, K. Harrabi, G. Fitch, D. G. Cory, Y. Nakamura, J. S. Tsai, and W. D. Oliver, Noise spectroscopy through dynamical decoupling with a superconducting flux qubit, Nature Physics **7**, 10.1038/nphys1994 (2011).
  - [14] E. Magesan, J. M. Gambetta, B. R. Johnson, C. A. Ryan, J. M. Chow, S. T. Merkel, M. P. Da Silva, G. A. Keefe, M. B. Rothwell, T. A. Ohki, M. B. Ketchen, and M. Steffen, Efficient measurement of quantum gate error by interleaved randomized benchmarking, Physical Review Letters **109** (2012).
  - [15] J. Kelly, R. Barends, B. Campbell, Y. Chen, Z. Chen, B. Chiaro, A. Dunsworth, A. G. Fowler, I. C. Hoi, E. Jeffrey, A. Megrant, J. Mutus, C. Neill, P. J. O’Malley, C. Quintana, P. Roushan, D. Sank, A. Vainsencher, J. Wenner, T. C. White, A. N. Cleland, and J. M. Martinis, Optimal quantum control using randomized benchmarking, Physical Review Letters **112**, 10.1103/PhysRevLett.112.240504 (2014).